coatings

MDPI

Article

Effect of Zinc Powder Reduced Graphene Oxide on the Corrosion Resistance of Waterborne Inorganic Zinc-Rich Coatings

Xuefei Fang [1], Yuchun Yuan [1,*], Qiuyue Wang [1,2,*], Chengwei Ji [1], Yuna Wu [1], Huan Liu [1], Jinghua Jiang [1] and Aibin Ma [1]

[1] College of Materials Science and Engineering, Hohai University, Changzhou 213000, China; xuefei_fang@163.com (X.F.); chengwei_ji@163.com (C.J.); wuyuna@hhu.edu.cn (Y.W.); liuhuanseu@hhu.edu.cn (H.L.); jinghua-jiang@hhu.edu.cn (J.J.); aibin-ma@hhu.edu.cn (A.M.)
[2] School of Naval Architecture & Ocean Engineering, Jiangsu Maritime Institute, Nanjing 211100, China
* Correspondence: ycyuan@hhu.edu.cn (Y.Y.); wangqiuyue@jmi.com.cn (Q.W.)

Abstract: Graphene oxide (GO) is considered an ideal material for applications involving corrosion resistance due to its excellent properties. However, the structure, surface functional groups, and distribution of GO in zinc-rich coatings (ZRCs) have a remarkable influence on coating properties. GO was reduced in a hydrochloric acid environment using spherical zinc powder, and the resulting products were subsequently dried and incorporated into waterborne inorganic ZRCs. Results show that zinc powder effectively reduces oxygen-containing functional groups on the GO surface, and reduced GO (rGO) is deposited on the surface of zinc powder. This improves the electron migration efficiency of rGO and decreases its surface energy. The electrochemical impedance spectroscopy (EIS) and salt spray test results demonstrate that among the coatings, the ZRC containing 0.2 wt.% rGO (40Zn–0.2rGO) exhibits the highest impedance modulus at the low frequency end. Its impedance modulus reaches 1×10^4 Ω·cm^2 after 216 h immersion. Furthermore, 40Zn–0.2rGO exhibits no signs of corrosion at the marked areas even after 216 h of the salt spray test. The good dispersion effect of the added 0.2 wt.% rGO in the coating, coupled with its exceptional electrical conductivity, facilitates the enhanced contribution of zinc powder to cathodic protection, thereby mitigating the matrix erosion caused by corrosive media. Following zinc powder corrosion, the surface of the coating can still be adorned with insoluble corrosion products such as ZnO or $Zn_5(OH)_8Cl_2$, thereby offering shielding protection to the substrate.

Keywords: waterborne inorganic zinc-rich coating; reduced graphene oxide; corrosion resistance; cathodic protection; shielding protection

check for updates

Citation: Fang, X.; Yuan, Y.; Wang, Q.; Ji, C.; Wu, Y.; Liu, H.; Jiang, J.; Ma, A. Effect of Zinc Powder Reduced Graphene Oxide on the Corrosion Resistance of Waterborne Inorganic Zinc-Rich Coatings. *Coatings* **2024**, *14*, 1321. https://doi.org/10.3390/coatings14101321

Academic Editor: Ludmila B. Boinovich

Received: 9 September 2024
Revised: 30 September 2024
Accepted: 4 October 2024
Published: 16 October 2024

Copyright: © 2024 by the authors. Licensee MDPI, Basel, Switzerland. This article is an open access article distributed under the terms and conditions of the Creative Commons Attribution (CC BY) license (https://creativecommons.org/licenses/by/4.0/).

1. Introduction

In marine engineering structural components, vehicles, ships, aircraft, and various steel structure engineering facilities on land, only a fraction of stainless steel can produce passivation layers without the need for special protection [1,2]. In addition, low-alloy steel, which is widely utilized for its commendable weldability, cutting performance, and exceptional toughness, necessitates subsequent protection due to its limited alloy content and inadequate passivation against corrosive environments [2,3]. The application of coatings represents a cost-effective and practical approach for safeguarding the surface integrity of steel structures against corrosion [4]. Waterborne inorganic zinc-rich coatings (ZRCs) have garnered considerable attention among a plethora of anti-corrosion coatings due to their rapid drying rate, non-toxic nature, and environmental friendliness [1,4,5]. However, the performance of ZRCs primarily relies on the zinc powder content, and an excessive amount of zinc powder can lead to reduced adhesion between the coating and the matrix, increased resource consumption, and other associated issues [6–9]. The incorporation of suitable functional fillers into ZRCs to optimize the utilization

of zinc powder and enhance their corrosion resistance has emerged as a prominent research focus [10–12].

Graphene oxide (GO) is regarded as an ideal material in the field of corrosion prevention due to its outstanding properties such as impermeability, high electron mobility, and thermal stability [13–15]. However, its structure, surface functional groups, and distribution state in ZRCs exert substantial influence on coating properties, necessitating further investigation in relevant studies. In 2021, Yong Tian et al. [16] modified GO using sulfonated multiwall carbon nanotubes (SMWCNTs). This approach resulted in the formation of SMWCNT-modified GO (SM-GO). Their results suggest that GO was effectively non-covalently modified by SMWCNTs. In SM-GO, interlayer spacing increased, and the dispersal quality is enhanced. The addition of GO, SWCNTs, and the resulting SM-GO facilitates enhanced electrical connectivity between zinc particles and the underlying metallic substrates, thereby augmenting the corrosion-preventive properties. The same year witnessed the design of a heterojunction structure by Lu Shen et al. [17]. In this structure, highly conductive MXene (Ti_3C_2) was grafted onto GO nanosheets. The addition of 0.5 wt.% Ti_3C_2 or GO-Ti_3C_2 to an epoxy ZRC proved to be effective in improving cathodic protection. In addition, the incorporation of GO-Ti_3C_2 into ZRC conferred remarkable corrosion resistance properties because GO-Ti_3C_2 in the coating enhanced the efficient utilization of zinc particles, while GO offered shielding protection against the spread of corrosives. In 2023, Wenhui Sun et al. [18] synthesized GO@(PDA+KH-550-Zn) nanocomposites fabricated by grafting dopamine (DA) onto a GO backbone via a silane coupling agent (KH-550), followed by the loading of zinc ions to enhance their properties. Upon penetration of the electrolyte into the coating matrix, the migration of zinc ions facilitated the development of oxide layers along the crack interfaces, while the polymerized diacrylate (PDA) matrix effectively immobilized ferrous or trivalent iron cations (Fe^{2+}/Fe^{3+}), thereby enhancing its adhesive and cohesive properties through the self-repairing mechanism. However, currently, the majority of research focuses on organic or waterborne epoxy ZRCs, giving limited attention to waterborne inorganic ZRCs that possess superior environmental attributes. The introduction of oxygen-containing functional groups into GO disrupts the pristine two-dimensional structure of graphene, leading to electron scattering and localized changes in charge distribution [19]. Consequently, this effect hampers electron mobility and charge carrier transport, thereby diminishing conductivity.

In this study, GO is employed as the precursor material, and spherical zinc powder is selected for its reduction in an acidic environment. This approach aims to effectively diminish the presence of oxygen-containing functional groups on the surface of GO and enhance electrical conductivity. The waterborne inorganic ZRC base material is prepared by incorporating a small amount of organic emulsion into lithium silicate solution and then adding reduced GO (rGO) at varying concentrations. This study investigates the effect of different rGO additions on the corrosion resistance of the waterborne inorganic ZRCs, thereby expanding the technical approach for graphene-based anti-corrosion applications and helping develop high-performance and environmentally sustainable anti-corrosion coatings.

2. Experimental

2.1. Materials

Q235 mild carbon steel specimens, measuring 200 mm × 100 mm × 2 mm, were procured from Anhui Gangtong Steel Co., Ltd. GO was sourced from Suzhou Tanfeng Graphene Technology Co., Ltd., Suzhou, China. Spherical and flake zinc powders, with particle sizes of 5–10 μm, were supplied by Xiamen Empire New Material Technology Co., Ltd., Xiamen, China. Lithium silicate solution was obtained from Linyi Lusen Chemical Co., Ltd., Linyi, China, whereas silicone acrylic emulsion was purchased from Beijing Donglian Chemical Co., Ltd., Beijing, China. The defoaming agent BYK-024 and dispersant BYK-110 were provided by BYK-Chemie GmbH (Berthelsdorf, Germany). The film-forming agent OE-300 was acquired from Eastman Material Innovation Company (Keansburg, NJ, USA).

Hydrochloric acid, anhydrous ethanol, distilled water, and sodium chloride (NaCl), all of analytical grade, were supplied by Chengdu Chron Chemical Co., Ltd., Chengdu, China. All reagents utilized in this study were of analytical grade, ensuring the highest purity for experimental accuracy.

2.2. rGO Preparation

Initially, quantitative GO was completely dispersed in a beaker containing 200 mL of distilled water using an electric mixer at 500 rev/min. The pH of the dispersion was adjusted to pH ≈ 4 with hydrochloric acid. The weak acidity solution was conducive to removing the thin oxide layer on the surface of zinc powder particles. The specific chemical formula for this reaction is

$$ZnO + 2HCl \rightarrow ZnCl_2 + H_2O$$

Subsequently, spherical zinc powder with particle sizes ranging from 5 to 10 μm and a mass ratio of 1:4 to GO was introduced into the beaker and stirred for 30 min. Upon observation, the original earthy-yellow solution of GO transformed into a colorless transparent solution as GO was reduced and coated by zinc powder, eventually settling at the bottom along with zinc powder. The excess solution was filtered through filter paper, whereas the resulting mixture was transferred to another beaker containing 200 mL of anhydrous ethanol and magnetically stirred for 3 min. This step was repeated two to three times to minimize water content. Finally, the mixture was vacuum-dried in an oven for 6–8 h before retrieval for further use.

2.3. Coating Preparation

A Q235 steel plate, measuring 100 mm × 200 mm × 2 mm, was processed using an electric spark wire cutting machine to prepare samples with dimensions of 10 mm × 10 mm × 2 mm and 30 mm × 30 mm × 2 mm. Subsequently, the surface of the samples was sequentially polished using silicon carbide sandpaper with mesh sizes of 200#, 400#, 800#, and 1000#. The polished samples were then ultrasonically cleaned in anhydrous ethanol for decontamination and oil removal and dried in a 60 °C air oven for 6–8 h. Finally, the samples were removed from the oven and sandblasted in accordance with ASTM D609 standards, resulting in $Sa2_{1/2}$ surface roughness.

Quantitative lithium silicate solution was added into a beaker, and silicon acrylic emulsion with a mass ratio of 4:1 to the lithium silicate solution was slowly added into the beaker at a rate of one drop per second while being stirred with an electric mixer for 30 min at 500 rev/min. During stirring, the defoamer, film forming agent, and dispersant were added in turn, and the solution changed from colorless to cream white in color. Subsequently, the rGO prepared in the previous step (0.1–0.4 wt.%) and 5–10 μm flake zinc powder were slowly added in turn and stirred at a high speed of 1200 rev/min for 30 min. An appropriate amount of distilled water was added during the process until the coating was evenly dispersed. The required test coating can thus be obtained. The sample naming format is 40Zn–XrGO, where X is the mass percentage of the amount of rGO added. The specific sample names and coating configurations are shown in Table 1.

Table 1. Raw material ratio of the rGO composite waterborne inorganic zinc-rich coatings.

Sample	Zinc (wt.%)	Binder (wt.%)	Additive&H_2O (wt.%)	rGO (wt.%)
40Zn	40	38	22	0
40Zn–0.1rGO	40	38	21.9	0.1
40Zn–0.2rGO	40	38	21.8	0.2
40Zn–0.3rGO	40	38	21.7	0.3
40Zn–0.4rGO	40	38	21.6	0.4

The coating was applied onto the prepared Q235 mild steel surface with dimensions 30 mm × 30 mm × 2 mm and 10 mm × 10 mm × 2 mm using a 50 μm wire rod coater. The thickness of the coating after curing at room temperature for 7 d was measured to be 50 ± 5 μm using a coating thickness gauge.

2.4. Characterization

Herein, the coating thickness was measured using the coating thickness gauge with 0.1 μm measurement accuracy (EC-770, Yuwen Measurement Technology Co., Ltd., Shenzhen, China). Raman spectroscopy (HORIBA Scientific LabRAM HR Evolution, Kyoto, Japan) was performed with a laser wavelength of 532 nm and a spectral resolution of 0.6 cm^{-1} to characterize the degree of GO reduction. The test wave number range was set at 500–4000 cm^{-1}, and random points were selected for testing. The micromorphology of GO and its modifications, as well as the changes in the surface micromorphology of the ZRCs before and after corrosion, were investigated using a scanning electron microscope (SEM, Hitachi Regulus 8100, Tokyo, Japan) in combination with energy-dispersive X-ray spectroscopy (EDS). An accelerating voltage of 15 kV and a scanning range of 5°–90° were applied during SEM. Furthermore, EDS was conducted to characterize the distribution of main elements within the coatings after immersion. The composition of corrosion products was analyzed through X-ray diffractometry (XRD, Rigaku Ultima IV, Akishima-shi, Japan). The scanning range was 5°–90° with a scanning speed of 10°/min. The obtained data were processed using Jade6 software. X-ray photoelectron spectroscopy (XPS, Thermo Scientific K-Alpha United States, Waltham, MA, USA) was employed with an Al Kα microfocusing monochromatic source as the X-ray source. The composition and chemical structure of coating corrosion products were determined by employing C 1s as the standard peak for correction. Avantage software was utilized for subpeak fitting.

2.5. Electrochemical Measurements

Electrochemical impedance spectroscopy (EIS) was performed using a CHI660E electrochemical workstation equipped with three electrodes. A saturated mercuric chloride electrode served as the reference electrode in a 3.5 wt.% NaCl solution. The auxiliary electrode comprised platinum, and the working electrode was a sample coated with waterborne inorganic ZRCs measuring 10 mm × 10 mm × 2 mm. All samples were connected using copper wires and securely fixed with epoxy resin, ensuring that only the coating layer remained exposed. Prior to testing, each test sample was immersed for 15–20 min in the 3.5 wt.% NaCl solution.

The open circuit potential (OCP) values of all samples were measured at different soaking times and recorded when fluctuations were less than 10 mV. EIS measurements were performed at the OCP value of the recorded sample in the frequency range of 10^{-2}–10^{5} Hz, with a sine wave amplitude of 10 mV and a signal acquisition frequency of 10 recordings per 10 times the frequency. The measured impedance data were analyzed using ZSimpWin software to obtain the relevant information of the corrosion process. All tests were conducted at approximately 25 °C, and three parallel samples were used for each type of coating to ensure repeatability of the tests.

2.6. Salt Spray Test

A coating sample, measuring 30 mm × 30 mm × 2 mm, was marked with an "X" on its surface. Its sides and back were sealed with epoxy resin to expose the coating layer only. The neutral salt spray test was conducted in a controlled environment chamber using a 5 wt.% NaCl solution (pH ≈ 6.5–7.2) at a temperature of 35 °C and an air pressure maintained between 0.1 and 0.2 MPa. Throughout the experiment, continuous testing was performed on the sample to ensure consistency and reliability of results. Three parallel samples were employed for each type of coating to guarantee repeatability.

3. Results and Discussion

3.1. Characterization of rGO Sheets

The surface microstructure of the spherical zinc powder before and after reduction of GO was characterized through SEM analysis, and the changes in the microstructures of the spherical zinc powder and GO were studied. Figure 1a illustrates that the spherical zinc powder exhibits a smooth and spherical surface with a diameter of approximately 8 µm. However, as depicted in Figure 1b, upon the reduction of GO by zinc powder, the surface of zinc powder is coated with numerous folded rGO sheets that are tightly interconnected to its surface due to the substitution reaction between zinc powder and H^+ in an acidic environment, resulting in the formation of Zn^{2+}. Subsequently, Zn^{2+} adsorbs onto the surface of the spherical zinc powder, rendering it positively charged. The oxygen atoms in the oxygen-containing functional groups on the surface of GO possess additional electrons, resulting in a negative charge (approximately −37 mV) [11,20]. This phenomenon can be ascribed to the higher electronegativity of oxygen than that of carbon, which attracts shared electron pairs and causes the accumulation of negative charges around carbon atoms. As a result of its negatively charged surface, GO exhibits electrostatic interactions with positively charged ions or molecules, being attracted to the positively charged spherical zinc powder surface and forming a coating structure. Despite having negative charges on its surface, GO still demonstrates a strong affinity for electrons and tends to receive electrons from external sources, consequently undergoing reduction. The specific chemical equation for the reduction of GO by zinc powder at this stage can be represented as

$$\mathrm{aGO} + \mathrm{bZn} \rightarrow \mathrm{arGO} + \mathrm{bZnO}.$$

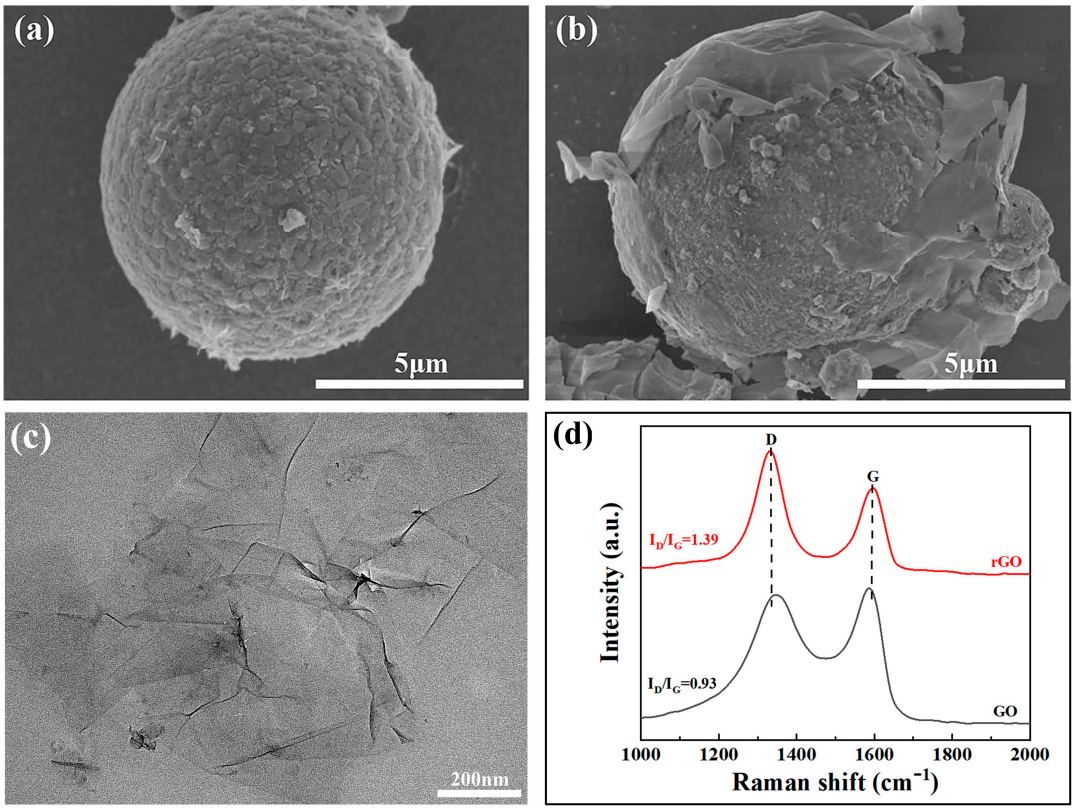


Figure 1. Characterizations of GO and rGO. SEM images of (**a**) pure zinc powder and (**b**) GO reduced by zinc powder; TEM images of (**c**) GO; and (**d**) Raman spectral results.

This process can also be interpreted as the dehydration and reduction of GO. In an acidic environment, hydrochloric acid provides a sufficient concentration of H^+. This situation leads to the dehydration reaction between the oxygen-containing functional

groups on the surface of GO and H^+. This reaction facilitates immediate charge transfer, resulting in the reduction of GO [21]. The specific chemical formula for this reaction is

$$GO + aH^+ + be^- \rightarrow rGO + cH_2O.$$

The TEM diagram in Figure 1c reveals the thinness of GO and its unique folded structure on its surface. This characteristic is attributed to the introduction of oxygen-containing functional groups during preparation. Raman spectroscopy was employed to characterize GO and rGO, enabling a microscopic investigation into the changes experienced by GO upon reduction by spherical zinc powder. The corresponding results are presented in Figure 1d. GO and rGO exhibit D peaks at approximately 1350 cm^{-1} Raman shift and G peaks at approximately 1580 cm^{-1} Raman shift [20,22,23]. The structural defects in GO can be qualitatively assessed by analyzing the peak intensity ratio (I_D/I_G) between D and G peaks. A high peak intensity ratio between D and G peaks is indicative of the high defect degree of GO, indicating complete reduction [20,22–24]. This phenomenon can be attributed to reductions in the average size of sp2 structure regions and the number of oxygen-containing functional groups on the surface of GO after reduction. The intensity ratio I_D/I_G of GO is 0.93, whereas that of rGO after zinc powder reduction is 1.39, which is higher than the I_D/I_G value of GO. These results suggest that GO has partially recovered.

3.2. Anti-Corrosion Performance of the Coatings

3.2.1. EIS Measurements

EIS is widely recognized as one of the most effective characterization methods for studying the corrosion of materials [25,26]. Herein, EIS was conducted to investigate whether the incorporation of zinc powder rGO can enhance the corrosion resistance of waterborne inorganic ZRCs and to determine the optimal quantity of rGO. Five different coatings were immersed in a 3.5 wt.% NaCl solution for 288 h and regularly subjected to EIS at various time intervals. The obtained test results were fitted with ZSimpwin software using the equivalent circuit diagram shown in Figure 2. The fitting outcomes align well with expectations. Herein, Rs represents the corrosive fluid resistance; Rc and Qc denote the coating resistance and the coating capacitance, respectively; and Rct and Qdl represent the charge transfer resistance and the double layer capacitance, respectively [27].

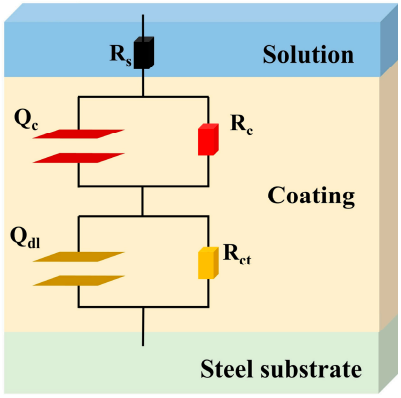


Figure 2. Equivalent circuit diagram of the numerical simulation of EIS measurements.

The fitting results of the Nyquist and Bode plots obtained after immersing the five coatings in the 3.5 wt.% NaCl solution are presented in Figure 3. A larger impedance arc radius in the Nyquist plot indicates that a coating has good corrosion resistance [27–29]. Comparing the Nyquist plots Figure 3a1–e1 reveals that the impedance arc radius of the 40Zn and 40Zn–0.1rGO gradually decreases with increasing immersion time, indicating that the corrosion resistance of these coatings gradually decreases as well. By contrast, the impedance arc radii of 40Zn–0.3rGO and 40Zn–0.4rGO initially increase and then decrease with increasing immersion time. The impedance arc radius of 40Zn–0.3rGO,

which has a slightly larger real part of impedance than 40Zn, reaches its maximum value at 72 h. However, the maximum real part of the impedance of 40Zn–0.4rGO is only 1170 $\Omega \cdot cm^2$, which is considerably smaller than that of 40Zn without rGO. This discrepancy may be attributed to the fact that while the excessive addition of rGO enhances electrical connectivity between the coating and the substrate to a certain extent, it also leads to agglomeration, resulting in defects, such as reduced adhesion and increased porosity within the carbon steel matrix–coating interface. Consequently, this effect diminishes the overall corrosion resistance of the coating. During prolonged immersion tests, only 40Zn–0.2rGO exhibits a notable enhancement in the corrosion resistance of the ZRCs. The impedance arc radius of the ZRC with 0.2 wt.% rGO gradually increases during 216 h of immersion. This phenomenon can be attributed to the improved electrical connection between zinc powder and the substrate, facilitated by the addition of an appropriate amount of rGO to the waterborne inorganic ZRC. Consequently, additional activated zinc powder participates in cathodic protection. Notably, the optimal addition of rGO ensures even dispersion within the coating, minimizing agglomeration and reducing porosity. Additionally, the timely coverage of holes by corrosion products resulting from the reaction of zinc powder enhances the shielding effect of the waterborne ZRC.

The Bode plots (frequency-phase angle) of Figure 3a2–e2 reveal the presence of two time constants, indicating that the erosive fluid undergoes two stages of cathodic protection and coating shielding protection. In the Bode (frequency–modulus) diagram, the impedance modulus at the low frequency end serves as a crucial indicator for assessing the impermeability of coatings. A high impedance modulus at the low frequency end (f = 0.01 Hz) corresponds to good barrier properties, whereas a low value indicates poor performance [29–31]. As depicted in Figure 3a3–e3, with the increase in immersion time, 40Zn and 40Zn–0.1rGO exhibit a gradual decrease in impedance moduli at their respective low frequency ends. The gradual increase in corrosion holes caused by immersion may contribute to this phenomenon because the corrosion products generated by the cathodic protection of zinc powder are insufficient for filling excessive corrosion pits, resulting in a gradual reduction in shielding protection performance. The low-frequency impedance moduli of 40Zn–0.3rGO and 40Zn–0.4rGO initially increase with immersion time but subsequently decrease possibly due to agglomeration resulting from the excessive addition of rGO to the coating. Although the corrosive medium can be partially isolated under the good impermeability of rGO, the negative effects caused by its defects become increasingly pronounced over time. Among the five coatings, only 40Zn–0.2rGO exhibits a low-frequency impedance modulus above 1×10^4 $\Omega \cdot cm^2$, likely due to the optimized dispersion of 0.2 wt.% rGO within the waterborne inorganic ZRCs. The excellent impermeability and large specific surface area of rGO enable prolonged contact between the corrosion medium and the carbon steel matrix. The appropriate addition of rGO not only enhances the electrical connection between zinc powder but also promotes the activation of additional zinc particles for cathodic protection. Consequently, this situation facilitates the complete coverage of corrosion pits and various holes by the resulting corrosion products. The low-frequency impedance modulus of 40Zn–0.2rGO gradually increases within 216 h prior to immersion and corrosion, providing further evidence for this phenomenon.

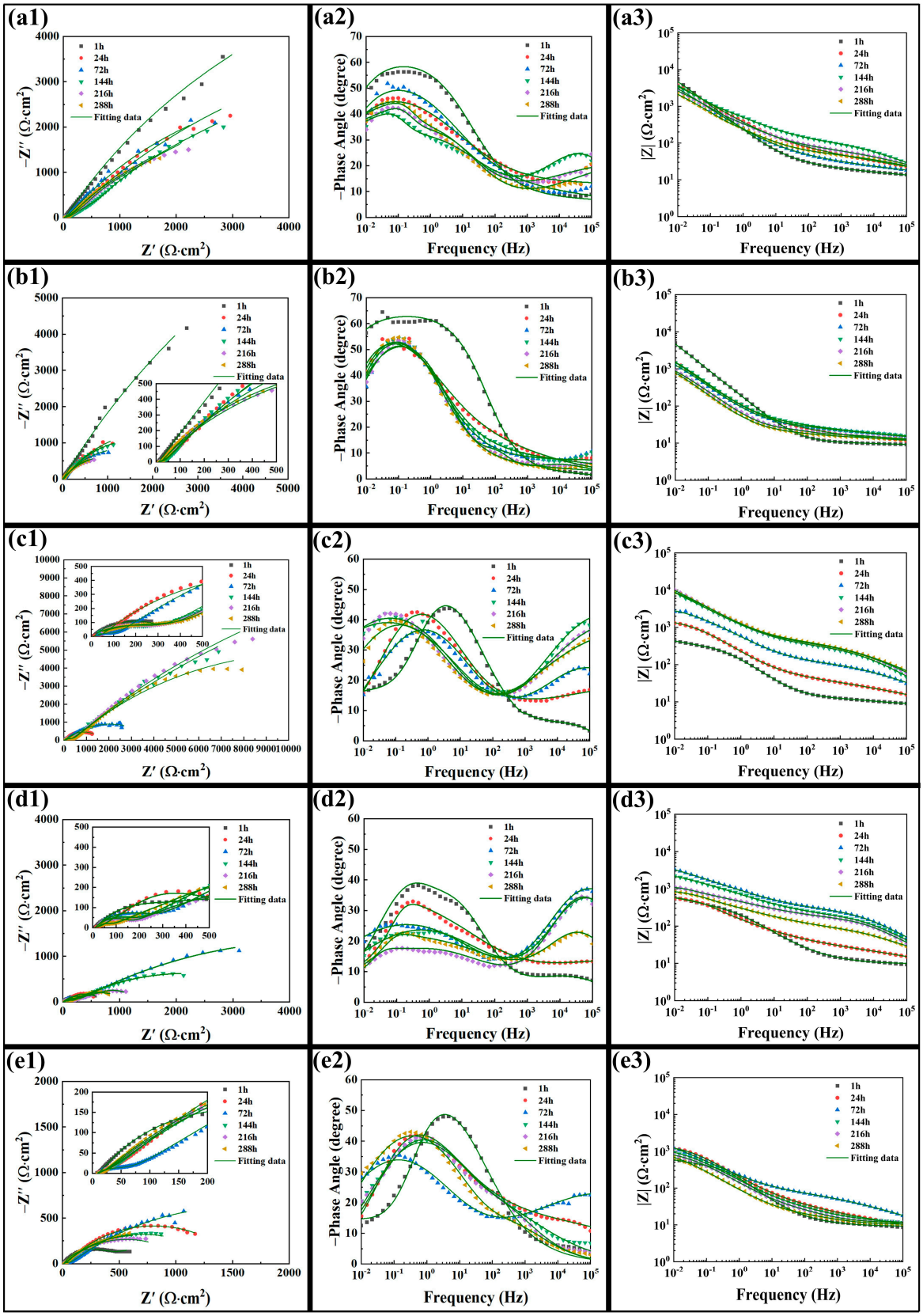


Figure 3. Nyquist and Bode plots of the composite ZRCs with different rGO addition levels at different time points during 288 h of immersion in a 3.5 wt.% NaCl solution: (**a1**,**a2**,**a3**) are 40Zn, (**b1**,**b2**,**b3**) are 40Zn–0.1rGO, (**c1**,**c2**,**c3**) are 40Zn–0.2rGO, (**d1**,**d2**,**d3**) are 40Zn–0.3rGO, and (**e1**,**e2**,**e3**) are 40Zn–0.4rGO.

3.2.2. Tafel Polarization Measurements

Figure 4 presents the Tafel polarization curves of the composite ZRCs with different rGO addition levels 72 h of immersion in a 3.5 wt.% NaCl solution. The Tafel polarization such as corrosion potential (E_{corr}), corrosion current density (i_{corr}), and cathodic and anodic Tafel slops (β_c and β_a) gathered from the Tafel plot by Tafel extrapolation method, as well as polarization resistance R_p, are listed in Table 2.

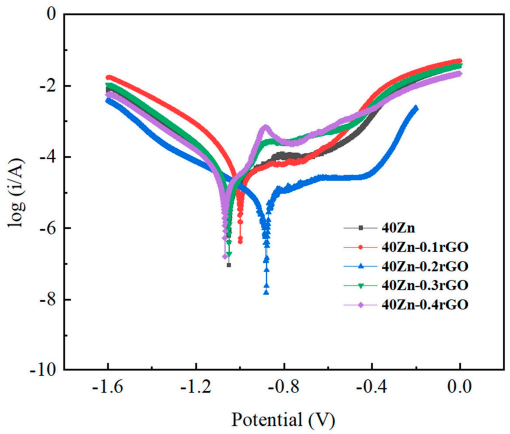


Figure 4. Tafel plots for 40Zn, 40Zn–0.1rGO, 40Zn–0.2rGO, 40Zn–0.3rGO, and 40Zn–0.4rGO samples after immersion in a 3.5 wt.% NaCl solution for 72 h.

Table 2. The electrochemical parameters of Tafel plots.

Sample	E_{corr} (mV)	I_{corr} (μA cm^{-2})	β_c (mV dec^{-1})	β_a (mV dec^{-1})	R_p (kΩ)
40Zn	−1052	0.196	7.672	3.412	2
40Zn–0.1rGO	−1054	0.166	7.88	7.046	1.752
40Zn–0.2rGO	−886	0.0464	4.815	7.296	5.852
40Zn–0.3rGO	−998	0.396	8.526	2.258	1.017
40Zn–0.4rGO	−1073	0.216	6.535	7.111	1.454

As shown in Figure 4, 40Zn–0.2rGO and 40Zn–0.1rGO make polarization curves shift to more positive values, but 40Zn–0.3rGO and 40Zn–0.4rGO shift to more negatively values compared with 40Zn. Among all the coatings, 40Zn–0.2rGO exhibits much positive E_{corr} and lower i_{corr}; furthermore, the R_p of 40Zn–0.2rGO is also higher than other coatings. This indicates that the anticorrosion property of 40Zn–0.2rGO is better than others, consistent with the results of EIS. Additionally, 40Zn–0.2rGO shows higher β_a values, confirming the inhibited anodic reaction.

3.2.3. Salt Spray Test

The macroscopic image of waterborne inorganic ZRCs with varying additions of rGO after exposure to neutral salt spray corrosion is presented in Figure 5. The coating without rGO (40Zn) exhibited corrosion under exposure to salt spray for 72 h, resulting in the presence of red rust in the marked area. Subsequently, after 144 h of corrosion, pitting is observed around the marked area, and the red rust gradually intensifies. At equivalent corrosion times, the amount of red rust on the coating added with 0.1 wt.% rGO (40Zn–0.1rGO) is slightly lower than that on the coating without rGO. Moreover, red rust only appears within the underlined region. Notably, the incorporation of 0.2 wt.% rGO (40Zn–0.2rGO) remarkably improves the corrosion resistance of ZRCs. In the initial 144 h, only white corrosion products, without any red rust, are observed on the coating surface. Subsequently, after 144 h, only a minimal amount of red rust is detected at the intersection points of lines likely because the incorporation of an appropriate quantity of rGO enhances the cathodic protection performance of the ZRC and mitigates the corrosion of the carbon steel substrate [32]. The white corrosion products on the coating surface simultaneously act as a barrier against the intrusion of corrosive media [33]. However, in the case of

40Zn–0.3rGO and 40Zn–0.4rGO, red rust extensively forms around the marked area 24 h prior to the salt spray test, gradually spreading thereafter likely because excessive rGO causes agglomeration, thereby increasing surface defects in the coatings and accelerating liquid erosion in the substrate [34].

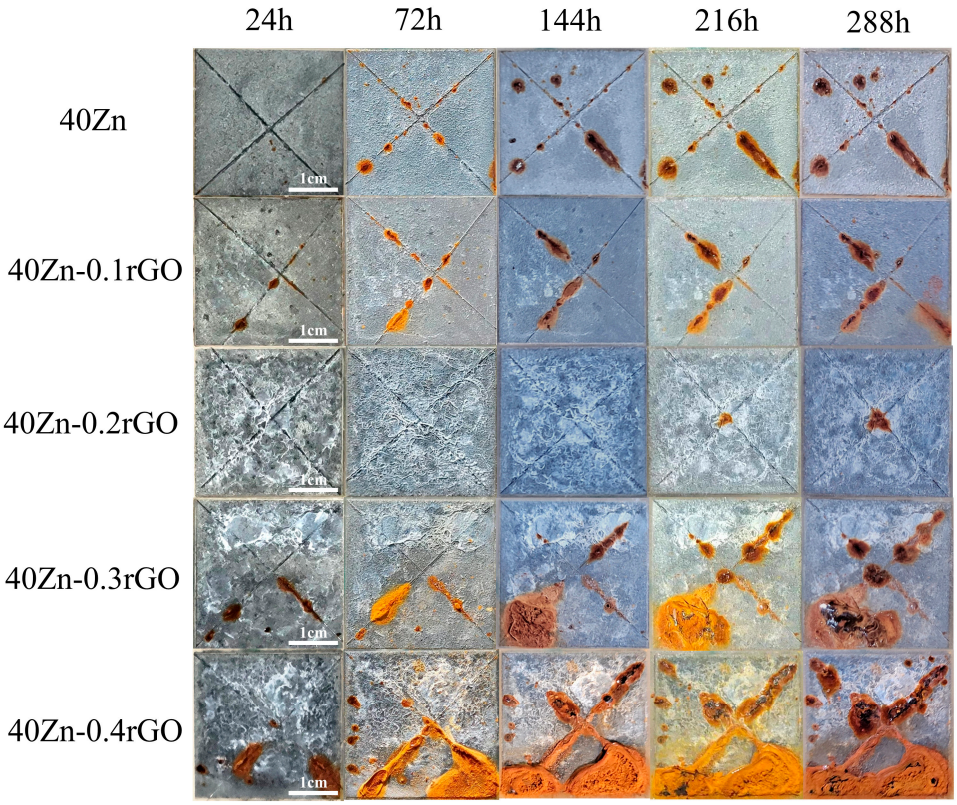


Figure 5. Optical images of five composite ZRCs under 288 h salt spray testing as a function of time.

3.3. Characterization of Corrosion Products

3.3.1. XRD and XPS

XRD is commonly used to determine the crystal phase composition and structure of substances, as well as the crystal arrangement of different elements in substances. The XRD results of 40Zn and 40Zn–0.2rGO before and after immersion in the 3.5 wt.% NaCl solution are presented in Figure 6. These results demonstrate that $Zn_5(OH)_8Cl_2$ serves as the primary corrosion product of both ZRCs. Notably, upon immersion, $Zn_5(OH)_8Cl_2$, an insoluble corrosion product, forms a protective layer on the coating surface, safeguarding the carbon steel substrate from exposure to the corrosive solution. Compared with that of 40Zn, the diffraction peak intensity of the corrosion product $Zn_5(OH)_8Cl_2$ of 40Zn–0.2rGO after 288 h of immersion is substantially enhanced likely due to the high activation rate of zinc powder in the waterborne inorganic ZRC with 0.2 wt.% rGO addition. This condition increases the involvement of zinc powder in cathodic protection through conductive pathways, resulting in the almost complete coverage of the carbon steel substrate by corrosion products and unreacted zinc powder. The addition of an appropriate amount of rGO is indirectly demonstrated to enhance the conductivity of the coating, reduce the quantity of zinc powder, and improve cathodic protection capability.

XPS is primarily employed to determine the binding energy of electrons, enabling the qualitative or quantitative analysis of the complete or detailed spectrum of surface substances. Such an analysis includes providing information on chemical state labelling, valence state determination, peak position identification, and other relevant details for fitting elements. Figure 6b illustrates the full XPS spectra of 40Zn and 40Zn–0.2rGO after 288 h of immersion and corrosion. As depicted in the figure, both samples exhibit similar

elemental compositions with the presence of Zn, C, O, and Cl. However, considerable amounts of Fe are detected on the surface of 40Zn after immersion and corrosion likely because of the loss of the protective effect of the waterborne inorganic ZRC on the carbon steel substrate when exposed to corrosive liquid conditions. Consequently, this finding indirectly suggests that incorporating ZRCs containing 0.2 wt.% rGO can provide enhanced protection to the underlying material during identical corrosion exposure periods.

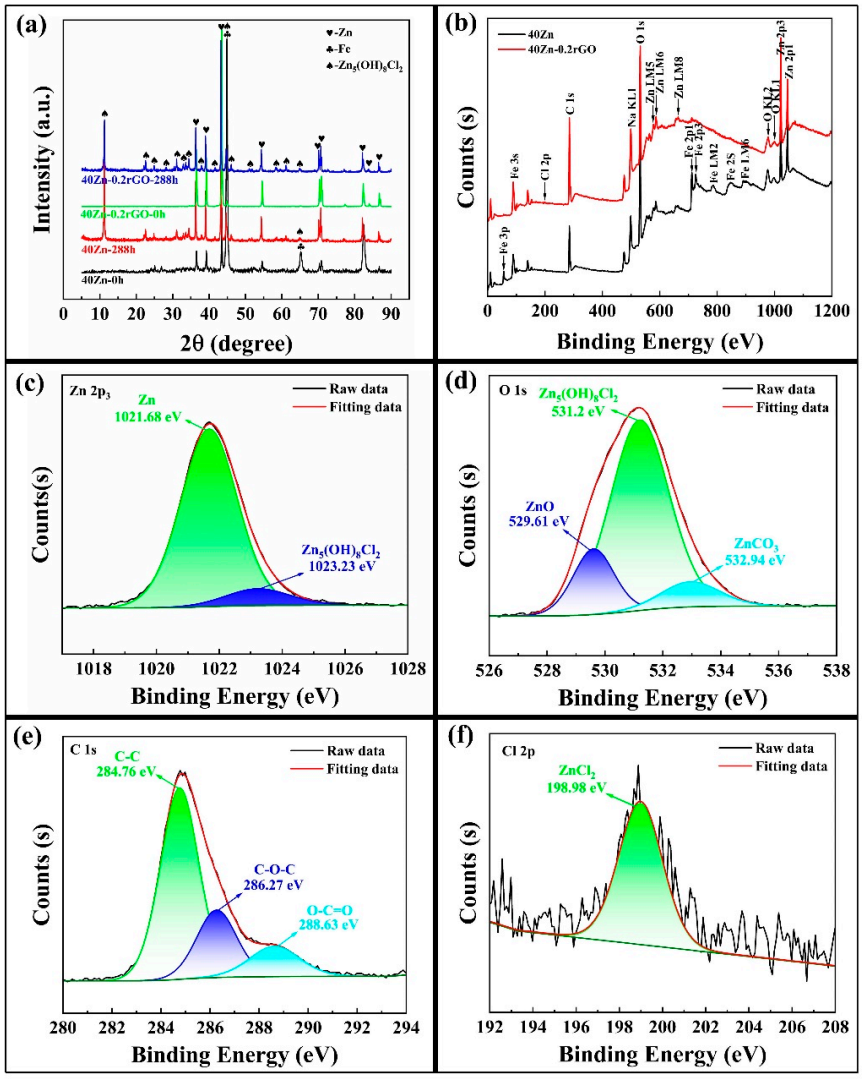


Figure 6. (**a**) XRD patterns and (**b**) XPS survey spectra of 40Zn and 40Zn–0.2rGO, (**c**) Zn $2p_3$, (**d**) O 1s, (**e**) C 1s, and (**f**) Cl 2p of high-resolution spectra of 40Zn–0.2rGO.

Figure 6c–f depict the XPS fine spectra of Zn, O, C, and Cl in 40Zn–0.2rGO following 288 h of immersion and corrosion, respectively. The XPS fine spectra in Figure 6c illustrate that Zn predominantly exists in the form of Zn and the corrosion product $Zn_5(OH)_8Cl_2$. In Figure 6d, O is present in the form of ZnO, ZnCO3, and $Zn_5(OH)_8Cl_2$. Meanwhile, in Figure 6f, Cl is observed in the form of $ZnCl_2$. This finding shows that the corrosion products generated by zinc powder exhibit a diverse range of chemical forms, indicating that not only $Zn_5(OH)_8Cl_2$ is present. In Figure 6e, the peak at 284.76 eV corresponds to the C–C bond, that at 286.27 eV can be attributed to the C–O–C bond, and that at 288.63 eV can be associated with the C–O=C bond present in $ZnCO_3$ [35]. On the basis of this result, the corrosion mechanism of zinc powder in the waterborne inorganic ZRC immersed in a 3.5 wt.% NaCl solution can be inferred as follows: Initially, the zinc powder present on the surface of the waterborne inorganic ZRC reacts with the Cl^- and OH^- groups generated by

H_2O decomposition within the corrosive environment, resulting in the formation of $ZnCl_2$ and $Zn(OH)_2$. Subsequently, a combination reaction between $ZnCl_2$ and $Zn(OH)_2$ leads to the production of $Zn_5(OH)_8Cl_2$. Furthermore, $Zn(OH)_2$ undergoes a reaction with the CO_2 present in air to generate $ZnCO_3$. This process not only demonstrates the sacrificial anodic protection of zinc powder but also actually enhances the binding force of the generated $ZnCO_3$ with the coating. This is because the consumption of zinc powder and the formation of zinc carbonate produce additional bonding effects in the coating, increasing the shielding effect of the coating, thus improving the binding force of the coating and the substrate. Additionally, the decomposition of $Zn(OH)_2$ yields ZnO [12].

$$Zn + 2Cl^- \rightarrow ZnCl_2 + 2e^-, \quad (1)$$

$$Zn + 2OH^- \rightarrow Zn(OH)_2 + 2e^-, \quad (2)$$

$$Zn(OH)_2 + CO_2 \rightarrow ZnCO_3 + H_2O, \quad (3)$$

$$4Zn(OH)_2 + 2ZnCl_2 \rightarrow Zn_5(OH)_8Cl_2, \quad (4)$$

$$Zn(OH)_2 \rightarrow ZnO + H_2O. \quad (5)$$

3.4. SEM-EDS

The micromorphology of waterborne inorganic ZRCs before and after immersion in a 3.5 wt.% NaCl solution was characterized using SEM. Figure 7a,b present the SEM images of 40Zn and 40Zn–0.2rGO prior to corrosion, respectively. 40Zn exhibits high porosity and low density, whereas 40Zn–0.2rGO demonstrates reduced pore formation with a dense arrangement of zinc powder, thus effectively preventing direct contact between the corrosive liquid and substrate. The SEM images of 40Zn and 40Zn–0.2rGO after 288 h of immersion and corrosion are shown in Figure 7c,d, respectively. The figure illustrates that severe corrosion has occurred on the surface of 40Zn, resulting in numerous corrosion pits and the loss of its protective function for the substrate material. By contrast, the surface of 40Zn–0.2rGO exhibits a considerable amount of corrosion products after immersion for an extended period of time relative to that before corrosion. These corrosion products fill up existing pores uniformly and densely, providing effective shielding against corrosive liquid intrusion to protect the substrate material [36,37].

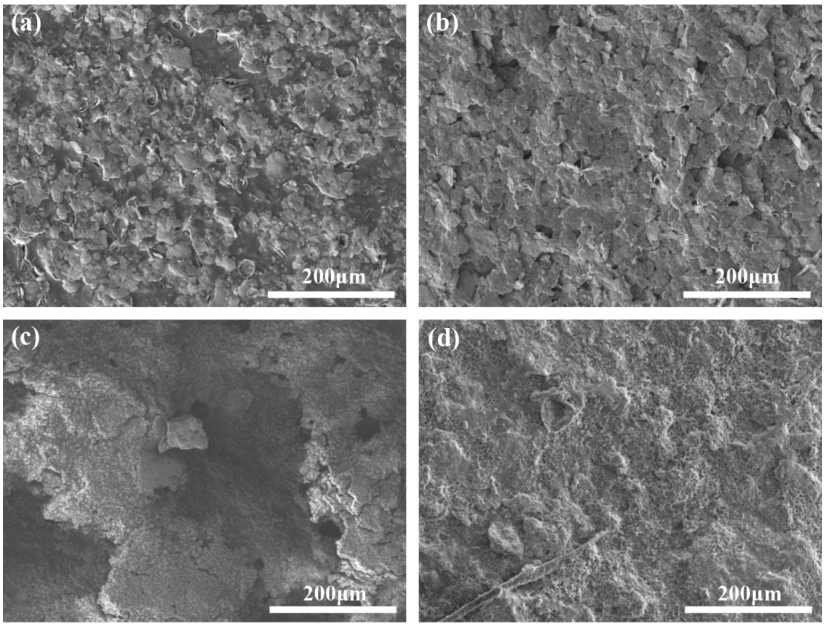


Figure 7. SEM images of 40Zn (**a**) before and (**c**) after 288 h of immersion and corrosion and of 40Zn–0.2rGO (**b**) before and (**d**) after 288 h of immersion and corrosion.

The surfaces of 40Zn and 40Zn–0.2rGO after 288 h of immersion in a 3.5 wt.% NaCl solution were examined through EDS to determine the distribution and proportion of each element within the coatings. Figure 8a presents the SEM image obtained after immersing 40Zn in a corrosive environment for 288 h. It reveals that despite the presence of corrosion products on the substrate's surface, numerous holes still exist. The elemental distribution in this region is represented by Zn, O, C, and Cl in Figure 8b–e, respectively. Figure 8f shows that the content of Zn is lower than that of Cl, with Cl atoms accounting for only 2.99% and 1.05%. Moreover, O and C have high proportions of 72.89% and 22.98%, respectively. The depletion of zinc powder in 40Zn that results in the formation of $Zn_5(OH)_8Cl_2$, ZnO, and other corrosion products may account for this phenomenon. These corrosion products have partially detached under the erosive action of the corrosive liquid, leaving some areas on the coating surface uncovered. Consequently, these remaining gaps facilitate the further penetration of the corrosive liquid into the substrate [38]. As a result, the protective properties of 40Zn for the matrix are drastically compromised.

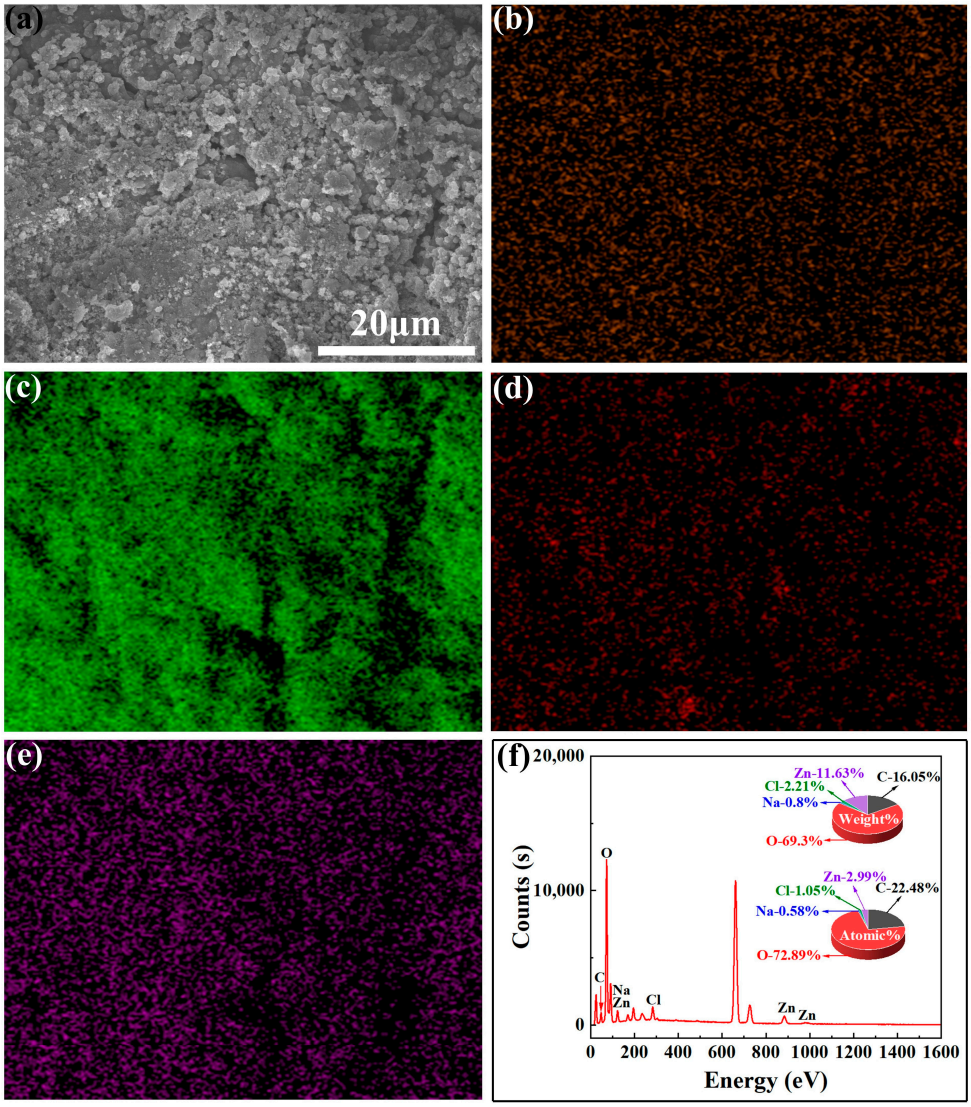


Figure 8. EDS maps of 40Zn after immersion in a 3.5 wt.% NaCl solution for 288 h. (**a**) SEM image of the scanning area. (**b**) Zn, (**c**) O, (**d**) C, (**e**) Cl, and (**f**) EDS results.

Figure 9a presents the SEM image of 40Zn–0.2rGO after 288 h of immersion. Despite the presence of a considerable amount of corrosion products on the surface of the ZRC, uncorroded flake zinc powder remains observable. These corrosion products effectively

fill the coating pores to form a dense protective layer [39]. Figure 9b–e present Zn and O. Figure 9f illustrates that the atomic proportion of Zn is 19.19%, which is approximately 17% higher than that observed in Figure 9 for pure zinc alone under identical corrosion time conditions. This finding indicates that even after exposure to corrosion for similar durations, 40Zn–0.2rGO can ensure the presence of high amounts of unreacted zinc powder or insoluble zinc corrosion products on the carbon steel substrate surface, thereby exhibiting enhanced corrosion resistance capabilities. This finding further suggests that the waterborne inorganic ZRC containing only 0.2 wt.% rGO can remarkably enhance anti-corrosion performance.

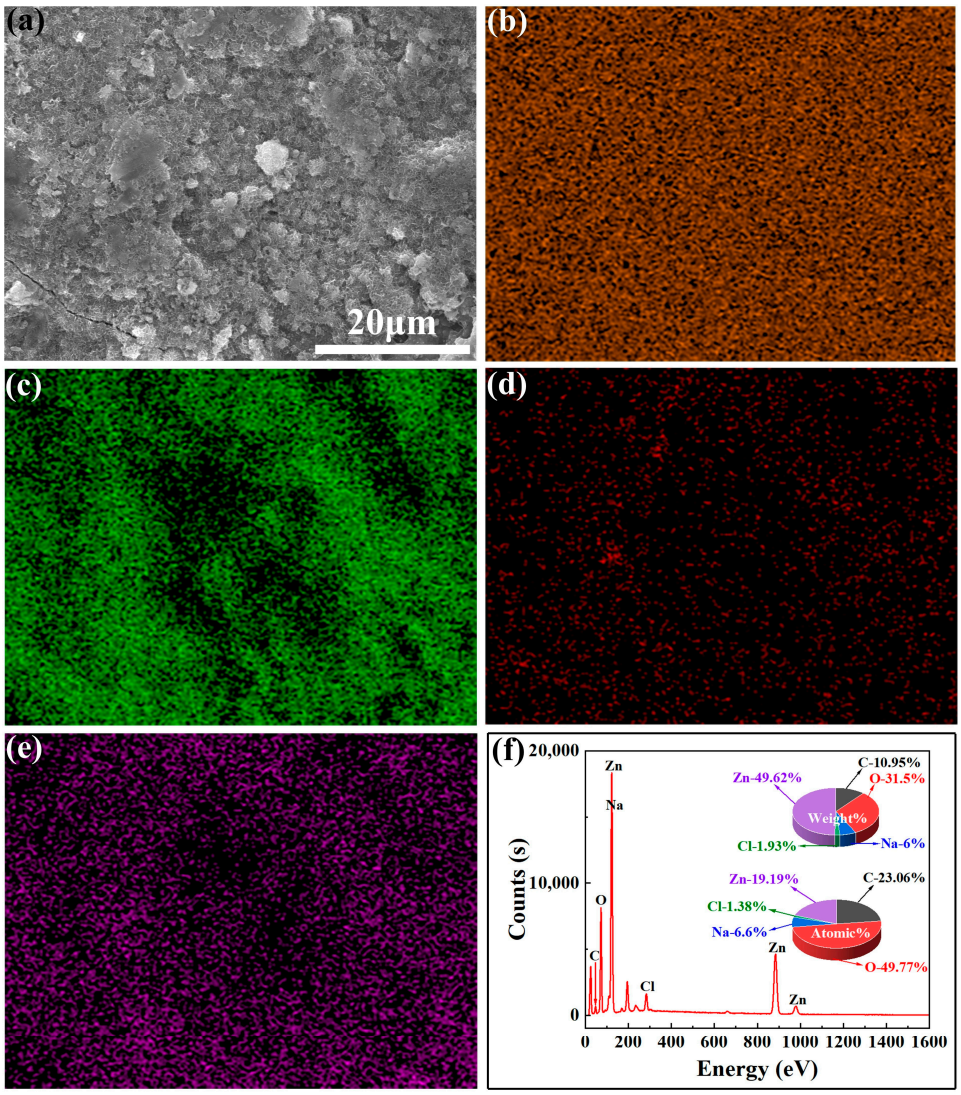


Figure 9. EDS mapping of 40Zn-0.2rGO after 288 h of immersion in a 3.5 wt.% NaCl solution. (**a**) SEM image of the scanning area. (**b**) Zn, (**c**) O, (**d**) C, (**e**) Cl and (**f**) EDS results.

4. Conclusions

In this study, GO was reduced using zinc powder in a hydrochloric acid environment, resulting in the successful preparation of a complex comprising rGO and zinc powder. Different proportions of rGO were then incorporated into a waterborne inorganic ZRC to create rGO composite coatings. The following results were obtained:

1. Spherical zinc powder reduces GO well in a hydrochloric acid environment. Raman spectroscopy results illustrate that GO has been restored to a high degree, and SEM images show the microscopic morphology of spherical zinc powder coated with rGO.

2. Although the electrical conductivity of ZRCs can be enhanced to a certain extent by incorporating rGO, agglomerations exist in the coatings when the additional amount of rGO exceeds 0.3 wt.%, leading to surface defects and a decline in the overall performance of the coatings.
3. At an rGO content of 0.2 wt.%, the anti-corrosion performance of 40Zn–0.2rGO surpasses that of other coatings due to the even dispersion of rGO, which reduces porosity and provides physical shielding against corrosive liquids. The addition of rGO also enhances the electrical connection between the coating and the substrate, improving cathodic protection and increasing the utilization rate of zinc powder without compromising corrosion resistance. XRD and XPS reveal that $Zn_5(OH)_8Cl_2$ is the primary corrosion product for aqueous inorganic ZRCs exposed to 3.5 wt.% NaCl solution. This insoluble corrosion product can provide shielding protection to the substrate.

Author Contributions: Conceptualization, X.F., Y.Y. and Q.W.; methodology, X.F.; software, H.L. and Y.W.; validation, X.F., Y.Y. and C.J.; formal analysis, X.F.; investigation, X.F.; resources, Y.Y. and Q.W.; data curation, X.F.; writing—original draft preparation, X.F.; writing—review and editing, X.F.; visualization, X.F.; supervision, J.J. and A.M.; project administration, Y.Y. and Q.W. All authors have read and agreed to the published version of the manuscript.

Funding: This research was funded by National Natural Science Foundation of China (Grant No. 51701065, 51979099), Jiangsu Maritime Institute Science and Technology Innovation Fund (Grant No. KJCX-1808), and Changzhou Dual Post Recruitment Programme (2024). The APC was funded by Nanjing Major Science and Technology Project (202309015) and Suqian Sucheng District Science and Technology Program Fund (Grant No. SC202204).

Institutional Review Board Statement: Not applicable.

Informed Consent Statement: Informed consent was obtained from all subjects involved in the study.

Data Availability Statement: The data that support the findings of this study are not openly available due to reasons of sensitivity and are available from the corresponding author upon reasonable request.

Conflicts of Interest: The authors declare no conflict of interest.

References

1. He, Y.; Illia, D.; Pan, J.; Anwar, A.; Tomas, D.; Corkery, R.W.; Claesson, P.M. Nano-scale mechanical and wear properties of a waterborne hydroxyacrylic-melamine anti-corrosion coating. *Appl. Surf. Sci.* **2018**, *457*, 548–558. [CrossRef]
2. Mahidashti, Z.; Shahrabi, T.; Ramezanzadeh, B. The role of post-treatment of an ecofriendly cerium nanostructure Conversion coating by green corrosion inhibitor on the adhesion and corrosion protection properties of the epoxy coating. *Prog. Org. Coat.* **2018**, *114*, 19–32. [CrossRef]
3. Jain, R.; Pitchumani, R. Fabrication and characterization of zinc based superhydrophobic coatings. *Surf. Coat. Technol.* **2018**, *337*, 223–231. [CrossRef]
4. Hussain, A.K.; Seetharamaiah, N.; Pichumani, M.; Chakra, C.S. Research progress in organic zinc rich primer coatings for cathodic protection of metals—A comprehensive review. *Prog. Org. Coat.* **2021**, *153*, 106040. [CrossRef]
5. Zhou, S.; Wu, Y.; Zhao, W.; Yu, J.; Jiang, F.; Wu, Y.; Ma, L. Designing reduced graphene oxide/zinc rich epoxy composite coatings for improving the anticorrosion performance of carbon steel substrate. *Mater. Des.* **2019**, *169*, 107694. [CrossRef]
6. Marchebois, H.; Keddam, M.; Savall, C.; Bernard, J.; Touzain, S. Zinc-rich powder coatings characterisation in artificial sea water: EIS analysis of the galvanic action. *Electrochim. Acta* **2004**, *49*, 1719–1729. [CrossRef]
7. Knudsen, O.Ø.; Steinsmo, U.; Bjordal, M. Zinc-rich primers—Test performance and electrochemical properties. *Prog. Org. Coat.* **2005**, *54*, 224–229. [CrossRef]
8. Ross, T.K.; Wolstenholme, J. Anti-corrosion properties of zinc dust paints. *Corros. Sci.* **1977**, *17*, 341–351. [CrossRef]
9. Arianpouya, N.; Shishesaz, M.; Arianpouya, M.; Nematollahi, M. Evaluation of synergistic effect of nanozinc/nanoclay additives on the corrosion performance of zinc-rich polyurethane nanocomposite coatings using electrochemical properties and salt spray testing. *Surf. Coat. Technol.* **2013**, *216*, 199–206. [CrossRef]
10. Lan, Y.; Cho, Y.; Liu, W.; Wong, W.; Sun, C.; Yeh, J. Small-load rGO as partial replacement for the large amount of zinc dust in epoxy zinc-rich composites applied in heavy-duty anticorrosion coatings. *Prog. Org. Coat.* **2023**, *175*, 107332. [CrossRef]

11. He, Y.; Han, S.; Zhao, G.; Luo, J.; Jia, C.; Chen, Y.; Liu, Q.; Gao, J.; Wang, C.; Wang, J. Zinc oxide-coated carboxyl-riched graphene oxide efficiently degrades microcystin-leucine arginine and antibiotics under visible light. *J. Environ. Chem. Eng.* **2022**, *10*, 107829. [CrossRef]
12. Qi, C.; Dam-Johansen, K.; Weinell, C.E.; Bi, H.; Wu, H. Enhanced anticorrosion performance of zinc rich epoxy coatings modified with stainless steel flakes. *Prog. Org. Coat.* **2022**, *163*, 106616. [CrossRef]
13. Jain, R.; Narayan, R.; Sasikala, S.P.; Lee, K.E.; Jung, H.J.; Kim, S.O. Phosphorene for energy and catalytic application—Filling the gap between graphene and 2D metal chalcogenides. *2D Mater.* **2017**, *4*, 042006. [CrossRef]
14. Husain, E.; Narayanan, T.N.; Taha-Tijerina, J.J.; Vinod, S.; Vajtai, R.; Ajayan, P.M. Marine corrosion protective coatings of hexagonal boron nitride thin films on stainless steel. *Appl. Mater. Interfaces* **2013**, *5*, 4129–4135. [CrossRef] [PubMed]
15. Jo, I.; Park, S.; Kim, D.J.; Moon, J.S.; Park, W.B.; Kim, T.H.; Kang, J.H.; Lee, W.; Kim, Y.; Lee, D.N. Tension-controlled single-crystallization of copper foils for roll-to-roll synthesis of high-quality graphene films. *2D Mater.* **2018**, *5*, 024002. [CrossRef]
16. Tian, Y.; Bi, Z.; Cui, G. Study on the Corrosion Resistance of Graphene Oxide-Based Epoxy Zinc-Rich Coatings. *Polymers* **2021**, *13*, 1657. [CrossRef]
17. Shen, L.; Zhao, W.; Wang, K.; Xu, J. GO-Ti$(_3)$C$(_2)$ two-dimensional heterojunction nanomaterial for anticorrosion enhancement of epoxy zinc-rich coatings. *J. Hazard. Mater.* **2021**, *417*, 126048. [CrossRef]
18. Sun, W.; Tang, E.; Zhao, L.; Yuan, M.; Liu, S.; Xing, X.; Liu, X. The waterborne epoxy composite coatings with modified graphene oxide nanosheet supported zinc ion and its self-healing anticorrosion properties. *Prog. Org. Coat.* **2023**, *182*, 107609. [CrossRef]
19. Tladi, B.C.; Swart, H.C.; Motaung, D.E.; Kroon, R.E. Effect of graphene oxide coatings on the optical properties of pulsed laser deposited ZnO:Zn thin films. *Opt. Mater.* **2023**, *146*, 114531. [CrossRef]
20. Chen, W.; Yan, L.; Bangal, P.R. Preparation of graphene by the rapid and mild thermal reduction of graphene oxide induced by microwaves. *Carbon* **2010**, *48*, 1146–1152. [CrossRef]
21. Zhou, M.; Wang, Y.; Zhai, Y.; Zhai, J.; Ren, W.; Wang, F.; Dong, S. Controlled synthesis of large-area and patterned electrochemically reduced graphene oxide films. *Chemistry* **2009**, *15*, 6116–6120. [CrossRef] [PubMed]
22. Shin, H.J.; Kim, K.K.; Benayad, A.; Yoon, S.M.; Park, H.K.; Jung, I.S.; Jin, M.H.; Jeong, H.K.; Kim, J.M.; Choi, J.Y. Efficient Reduction of Graphite Oxide by Sodium Borohydride and Its Effect on Electrical Conductance. *Adv. Funct. Mater.* **2009**, *19*, 1987–1992. [CrossRef]
23. Chen, D.; Li, L.; Guo, L. An environment-friendly preparation of reduced graphene oxide nanosheets via amino acid. *Nanotechnology* **2011**, *22*, 325601. [CrossRef]
24. Zhou, Y.; Bao, Q.; Tang, L.; Zhong, Y.; Loh, K.P. Hydrothermal Dehydration for the "Green" Reduction of Exfoliated Graphene Oxide to Graphene and Demonstration of Tunable Optical Limiting Properties. *Chem. Mater.* **2009**, *21*, 2950–2956. [CrossRef]
25. Yan, R.; He, W.; Zhai, T.; Ma, H. Corrosion protective performance of amino trimethylene phosphonic acid-metal complex layers fabricated on the cold-rolled steel substrate via one-step assembly. *Appl. Surf. Sci.* **2018**, *442*, 264–274. [CrossRef]
26. Ding, R.; Zheng, Y.; Yu, H.; Li, W.; Wang, X.; Gui, T. Study of water permeation dynamics and anti-corrosion mechanism of graphene/zinc coatings. *J. Alloys Compd.* **2018**, *748*, 481–495. [CrossRef]
27. Ding, R.; Wang, X.; Jiang, J.; Gui, T.; Li, W. Study on Evolution of Coating State and Role of Graphene in Graphene-Modified Low-Zinc Waterborne Epoxy Anticorrosion Coating by Electrochemical Impedance Spectroscopy. *J. Mater. Eng. Perform.* **2017**, *26*, 3319–3335. [CrossRef]
28. Marchebois, H.; Touzain, S.; Joiret, S.; Bernard, J.; Savall, C. Zinc-rich powder coatings corrosion in sea water: Influence of conductive pigments. *Prog. Org. Coat.* **2002**, *45*, 415–421. [CrossRef]
29. He, Z.; Cao, H.; Zhou, M.; Jia, W.; Shen, X.; Min, Y.; Xu, Q. Superior corrosion resistance and anti-biofouling performance via electrodeposited graphene oxide/silane composite coating with special wettability. *Surf. Coat. Technol.* **2022**, *449*, 128952. [CrossRef]
30. Ge, T.; Zhao, W.; Wu, X.; Lan, X.; Zhang, Y.; Qiang, Y.; He, Y. Incorporation of electroconductive carbon fibers to achieve enhanced anti-corrosion performance of zinc rich coatings. *J. Colloid Interface Sci.* **2020**, *567*, 113–125. [CrossRef]
31. Bai, W.; Ma, Y.; Meng, M.; Li, Y. The influence of graphene on the cathodic protection performance of zinc-rich epoxy coatings. *Prog. Org. Coat.* **2021**, *161*, 106456. [CrossRef]
32. Cao, X.; Huang, F.; Huang, C.; Liu, J.; Cheng, Y.F. Preparation of graphene nanoplate added zinc-rich epoxy coatings for enhanced sacrificial anode-based corrosion protection. *Corros. Sci.* **2019**, *159*, 108120. [CrossRef]
33. Arman, S.Y.; Ramezanzadeh, B.; Farghadani, S.; Mehdipour, M.; Rajabi, A. Application of the electrochemical noise to investigate the corrosion resistance of an epoxy zinc-rich coating loaded with lamellar aluminum and micaceous iron oxide particles. *Corros. Sci.* **2013**, *77*, 118–127. [CrossRef]
34. Jalili, M.; Rostami, M.; Ramezanzadeh, B. An investigation of the electrochemical action of the epoxy zinc-rich coatings containing surface modified aluminum nanoparticle. *Appl. Surf. Sci.* **2015**, *328*, 95–108. [CrossRef]
35. Mei, X.; Ouyang, J. Ultrasonication-assisted ultrafast reduction of graphene oxide by zinc powder at room temperature. *Carbon* **2011**, *49*, 5389–5397. [CrossRef]
36. Zhang, L.; Hou, G.; Zhai, W.; Ai, Q.; Feng, J.; Zhang, L.; Si, P.; Ci, L. Aluminum/graphene composites with enhanced heat-dissipation properties by in-situ reduction of graphene oxide on aluminum particles. *J. Alloys Compd.* **2018**, *748*, 854–860. [CrossRef]

37. Zhang, L.; Ma, A.; Jiang, J.; Song, D.; Chen, J.; Yang, D. Anti-corrosion performance of waterborne Zn-rich coating with modified silicon-based vehicle and lamellar Zn (Al) pigments. *Prog. Nat. Sci. Mater. Int.* **2012**, *22*, 326–333. [CrossRef]
38. Zhang, L.; Tong, X.; Lin, J.; Li, Y.; Wen, C. Enhanced corrosion resistance via phosphate conversion coating on pure Zn for medical applications. *Corros. Sci.* **2020**, *169*, 108602. [CrossRef]
39. Huang, J.; Yang, M.; Zhu, W.; Tang, K.; Zhang, H.; Chen, J.; Noël, J.J.; Barker, I.; Zhang, H.; Zhu, J. Extrusion-free fabrication of zinc-rich powder coatings: Press bonding. *Chem. Eng. J.* **2022**, *442*, 135925. [CrossRef]

Disclaimer/Publisher's Note: The statements, opinions and data contained in all publications are solely those of the individual author(s) and contributor(s) and not of MDPI and/or the editor(s). MDPI and/or the editor(s) disclaim responsibility for any injury to people or property resulting from any ideas, methods, instructions or products referred to in the content.